Chapter 7. Interpretations

This chapter combines the experimental insights of Chapters 2 to 6 and explains the hydrodynamic multiplicity trends in terms of a newly proposed multiplicity mechanism. In order to steer clear of empirical detail, the focus is firmly on a qualitative description of the observed trends. However, at the end of this chapter a clear strategy is outlined by which hydrodynamic multiplicity can be incorporated into existing hydrodynamic models. In terms of the overall strategy, this chapter addresses the Multiplicity Mechanism block in Figure 1 and Objective 3 of Chapter 3.

7.1 Introduction: Trends Revisited

In Chapters 2, 4, 5 and 6 a number of trends were pointed out that embodies the nature of hydrodynamic multiplicity and that should be described by a hydrodynamic multiplicity model. These were discussed in detail and the reader is referred to the many figures in these chapters. However, there are some issues and trends that are prominent in understanding hydrodynamic multiplicity. To recap, these are:

(A) There are different flow patterns in the different modes: rivulet-type flow in the lower limiting cases and film-type flow in the upper limiting cases. New rivulets are created as u_L increases.

(B) Liquid flow rate variation induced hysteresis causes increases in pressure drop and liquid holdup in the Non-pre-wetted and Levec modes.

(C) Gas flow rate variation induced hysteresis causes increases in pressure drop and holdup in the Levec mode, but an increase in holdup and a decrease in pressure drop in the Kan-Liquid mode.

(D) The extent of pressure drop hysteresis is diminished when particle size is increased.

(E) The Levec mode *wetting efficiency* is lower on average and shows a bi-modal particle wetting distribution, whereas the Super mode shows a Gaussian distribution.

(F) The liquid *holdup* increases by mode in the order Non-pre-wetted, Levec, Kan-Liquid/Super and then the Kan-Gas mode.

(G) The *pressure drop* for the Non-pre-wetted and Levec modes are the same and lower than the Kan-Liquid/Super mode pressure drop. The Kan-Gas pressure drop is in between these despite it having a *larger* holdup.

(H) The *volumetric gas-liquid mass transfer coefficient* shows the same functional behaviour as the pressure drop.

(I) The *Super and Kan-Liquid modes have similar behaviour*, both in the uniformity of the flow distribution and in the nearly identical values in all the hydrodynamic parameters - despite having been established with different operating procedures.

(J) *Small flow rate changes* have little effect on the hydrodynamic multiplicity after the first or second cycle.

(K) A *decrease in surface tension* brings the pulsing boundary to lower liquid velocity, but hydrodynamic multiplicity still persists in the trickle regime.

(L) A temporary decrease in the surface tension (*surface tension change induced hysteresis*) has no effect on the pressure drop in the Kan-Liquid mode but increases the pressure drop in the Levec mode.

(M) Beds of porous particles have a lower extent of multiplicity compared to beds of non-porous particles.

(N) The extent of multiplicity is associated with the pulsing boundary; *hysteresis is diminished if the pulsing boundary velocity is lowered* (by changing surface tension or particle shape).

(O) An increase in liquid or gas velocity in the *Levec mode drastically increases the pressure drop* at high pressure (gas density), while the increase in the other modes is far less drastic.

(P) High pressure operation (or high gas mass flux) has little effect on multiplicity at low liquid velocity, but decreases the extent of multiplicity at high liquid velocity. The *pressure drop determines the extent of multiplicity*.

(Q) *Time to steady state*: the Kan-Liquid mode takes longer to reach a steady flow pattern than the Levec mode.

(R) There are *particle scale low frequency flow pattern changes* in the Levec mode, but not in any of the other pre-wetted modes.

(S) The Levec mode *holdup distribution* is always bi-modal (and increasingly so as liquid velocity is increased). The Kan-Liquid mode is uni-modal at low velocity and bi-modal at the highest velocity. See Figure 59.

(T) The *fraction of pores that contain no dynamic liquid* in the Levec mode decreases from 12.7% to 5.5% and then to 0.2% as velocity rises from 1.3 to 2.7 to 5.3 mm/s. In the Kan-Liquid mode, this fraction is always approximately zero – even at low velocity (see Figure 60). Note also that increasing the gas velocity in the Levec mode results in a decrease in the fraction un-irrigated pores, despite also resulting in a decrease in holdup.

7.2 Proposed Mechanism

The proposed mechanism of liquid distribution is based on overcoming the surface forces at the pore necks (pore-to-pore connections). To start, consider the hydrostatic fate of a liquid droplet at the bottom end of a vertical conical capillary tube that is being filled with a liquid from the top (Figure 61a to Figure 61e). This discussion follows the simplified treatment of Middleman (1998:33-45). The forces on the liquid body are the gravitational body force and the surface tension forces at the top and bottom menisci. The liquid-solid surface tension is treated as a contact angle (defined as the angle between the

tangent to the liquid surface at the triple point and the solid surface, Ku et al., 1968). A force balance on the liquid volume yields:

$$\cos\theta' = -\frac{mg}{\sigma_{GL}\pi d} \qquad (22)$$

Now, when there is very little liquid in the tube, the gravitational force is small, and the top and bottom contact angles are equal (see Figure 61a). As the amount of liquid is increased, a droplet forms at the bottom of the capillary and the bottom contact angle increases to compensate for the additional weight (Figure 61b and Figure 61c). This continues until the contact angle reaches the *critical contact angle* (which may be as high as 180^{o} but is often taken as the *advancing* contact angle, Meister & Latychevskaia, 2006), at which point the drop detaches. This yields the familiar result that the droplet detaches when the gravity and surface forces are equal (ratio of 1) and the bottom contact angle is a maximum (Middleman, 1998:34). The shape of the droplet can be solved for from the Young-Laplace equation (Meister & Latychevskaia, 2006), but it is not important for the present purposes. If we continue to supply liquid to the top, a steady flow will be established (Figure 61d). If the liquid supply is then decreased, the contact angle decreases until it reaches the *receding contact angle*, at which point the flow stops. Now, it is well established that the receding contacting angle is smaller than the advancing one (see for example Bear, 1974). This means that the capillary exit acts like a gate that is blocked by capillary pressure and is only opened when the hydrostatic pressure exceeds the capillary pressure value associated with the critical/advancing contact angle: $(4\sigma/d)\cos\theta'_{crit}$. The gate closes when the hydrostatic pressure drops below $(4\sigma/d)\cos\theta'_{rec}$. For hydrostatic pressures in the range $(4\sigma/d)\cos\theta'_{rec}$ to $(4\sigma/d)\cos\theta'_{crit}$, the gate is either open (if the hydrostatic pressure had exceeded the critical value in its history) or closed (if it had not).

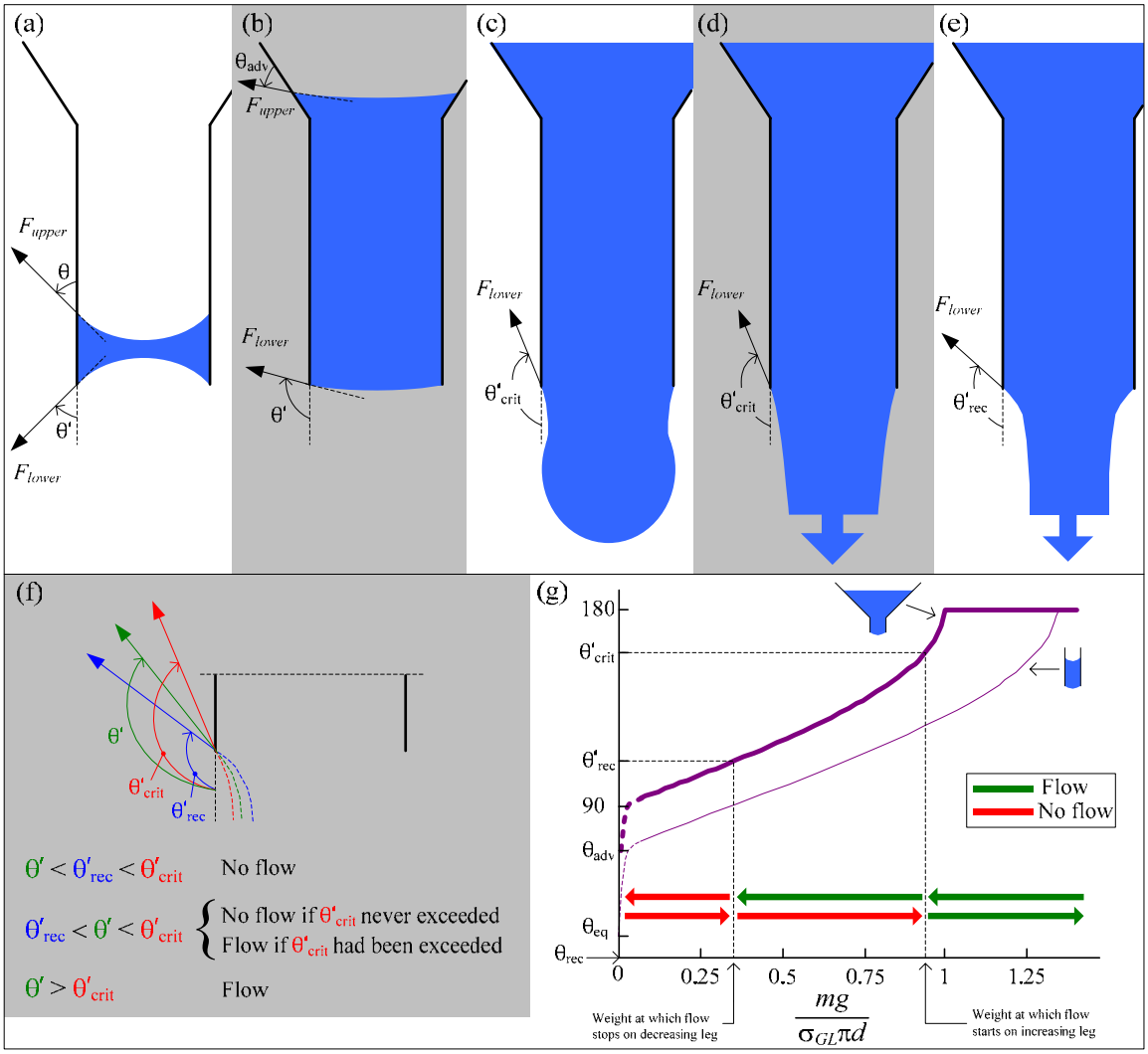

Figure 61. Liquid suspended by capillary force in a vertical conical capillary tube. (a)-(c) Menisci shapes as the weight in the tube increases (d) Just after the critical contact angle is exceeded (e) As flow rate is reduced θ' decreases until the flow stops at θ'$_{rec}$ (f) The fringe region enlarged (g) Bottom contact angle as a function of weight - showing the weight to capillary force regions where the gate is closed (red) and open (green).

See Figure 61f. This behaviour was observed qualitatively with a 1 mm capillary in the laboratory. This is the crux of the proposed mechanism. It is illustrated in another way by the coloured lines in Figure 61g. Note that this is reminiscent of the stick-slip behaviour of control valves as well as the phenomenon of a static and a dynamic friction coefficient in rigid body dynamics. In fact, it is possible to reformulate the equations in terms of a

"retardation" coefficient that is a type of static friction coefficient analogue (Ku et al., 1968).

There are a variety of complications that may arise. The geometry of the capillary greatly influences the values of the bottom contact angle and therefore the range of hydrostatic pressures that can either induce flow or not. For example, if the capillary is straight (as opposed to conical at the top), the upper surface force is not negligible and the bottom contact angle changes with the ratio of gravity to surface force as shown by the thin line in Figure 61g. The value of the critical contact angle is another contestable point, although the fact that it is larger than the receding angle is well established. Another complication arises when there is a substrate close to the exit of the capillary (Figure 62, Ku et al., 1968). At first, capillary action keeps the liquid from forming a bridge by keeping it inside the capillary. Once the drop touches the substrate, a bridge is formed and the liquid flows freely. As liquid flow is reduced, the liquid column is supported also by the vertical component of the force ($F_{sub}\sin\theta''$) at the substrate, which means that θ' will not need to reduce as much as it did when there was no substrate (it takes a lower static head for θ' to reach θ'_{rec}, meaning θ' is larger at the same flow rate than it was when the substrate was not present). All this means that flow will continue for even lower hydrostatic heads (i.e. there are lower flow rates that can be maintained without the "gate" closing). The orientation of the tube (assumed to be vertical before) of course also impacts the situation. Note that viscous forces are neglected in this treatment and that the full dynamic case is more complex and somewhat less understood. The concepts introduced here are based mainly on hydrostatic considerations and this should be considered the major limitation of the idea.

From this brief discussion, it is evident that a fundamental treatment of capillary phenomena in the complex environment of a packed bed is beyond present capabilities. The proposed mechanism is a *phenomenological* one that still needs to be mapped to the bed and flow characteristics.

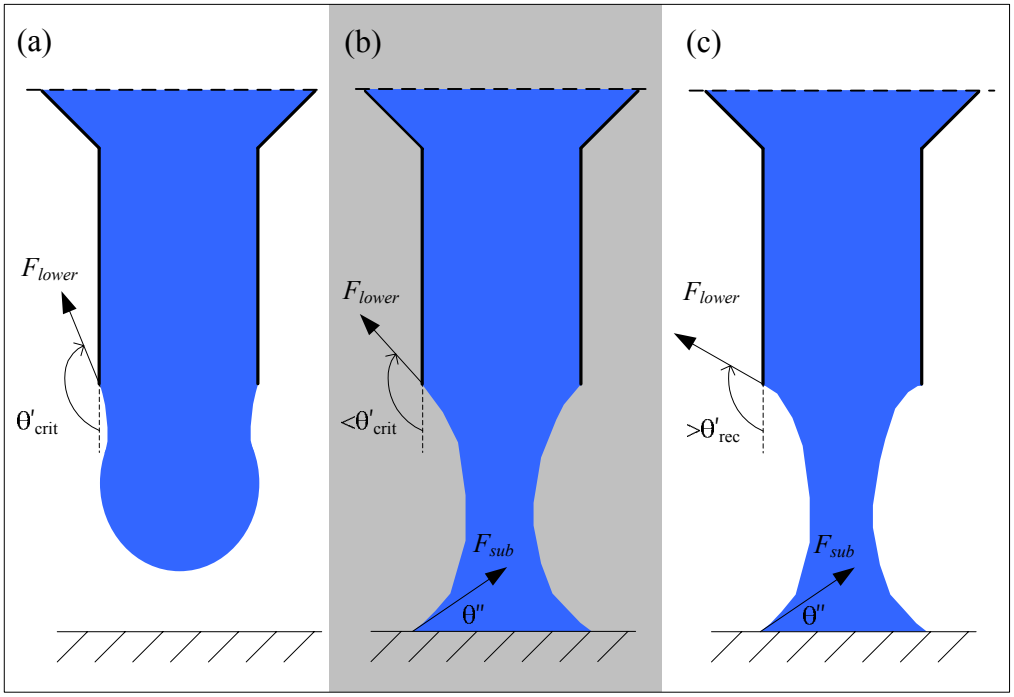

Figure 62. Liquid discharge from a vertical capillary in the presence of a substrate. (a) Droplet is critically poised (b) Just after liquid bridge was created (c) Liquid bridge at the weight where the flow in the substrate-less case stopped – flow persists down to smaller weights because the additional support allows θ' to take longer to reach θ'_{rec} as the weight is decreased.

Having considered these complexities, they are now reconciled with the desire to develop a simple yet effective model. It is proposed that adequate representation of this effect is the following:

- A capillary exit acts as a gate that is initially closed.
- The gate opens for flow when the pressure exceeds a critical value that is given by the capillary pressure at the advancing contact angle.
- When the pressure is reduced (by a reduction in the feed flow rate for example), the gate remains open until the pressure has dropped to below the capillary pressure at the receding contact angle.

7.3 Capillary Gate Model For Explaining Multiplicity Trends

In this section a capillary gate model based on the ideas of the previous section is developed. The objective is to apply a simplified version of the capillary effect to a simplified pore geometry in order to try to reproduce the multiplicity trends listed at the start of the chapter. An additional objective is that the model should also be able to capture hydrodynamic trends that are not specifically multiplicity related (as summarized in Chapter 2.1).

7.3.1 Model Development

The model is developed in three phases. First**,** the focus is on how the pores themselves should be represented (in particular the choice between viewing the pore as a tank or as a tube). In the next two phases the effect of capillary action on liquid flow and gas flow is considered.

Simplification of Pore Geometry: Tank vs. Tube

Note that there is no hysteresis for isothermal single phase flow. This suggests that hydrodynamic multiplicity is a consequence of interfacial surface forces. The first step toward understanding how these surface tension effects lead to the observed hydrodynamic multiplicity behaviour, is to recognize that each pore-pore connection or "neck" acts as a capillary exit or gate (and is therefore subject to the effect described in the previous section). A question that arises is whether a pore can be approximated by a *straight* capillary tube or a *conical* one. In the former, the exit diameter is comparable to the mean diameter, whereas for the latter the exit is much smaller than the mean. Note that this is also an important hydrodynamic question, namely whether the pores are to be represented as "tubes" (with pressure drop over its entire length – an approach adopted by most present hydrodynamic models) or "tanks" with constricted exits (with pressure drop

only over the exits because the fluid velocity in the pore is comparatively low). Consider the pressure drop over a tube with a constricted exit, where capillary actions have been neglected for the time being (it will be incorporated in the next two sections). As shown in Figure 63, the total pressure drop is the sum of the pressure drop over the length l and the pressure drop over the exit (which has an area of A_{exit}). If viscous laminar flow prevails in the tube, the pressure drop is given by the Hagen-Poiseuille equation (Welty et al., 1984), whereas the pressure drop over the exit can be deduced from a mechanical energy balance (Bernoulli's equation, where it is assumed that all the potential energy is converted to kinetic energy). This yields (subject to the assumptions of incompressible, steady Newtonian flow):

$$\begin{aligned}\left(\Delta P+\rho g l\right) &= \left(\frac{\Delta P}{l}\right)_{tube} l+\Delta P_{exit} \\ &= \left(\frac{32\mu u_{tube}}{d_t^2}\right) l+\frac{\rho u_{exit}^2}{2} \\ &= \frac{128\mu Q l}{\pi d_t^4}+\frac{\rho Q^2}{2A_{exit}^2}\end{aligned} \tag{23}$$

This equation closely resembles the Ergun (1952) equation for pressure drop in packed beds. The relative importance of the two contributions can be expressed in terms of their ratio (N):

$$N=\frac{256\mu l A_{exit}^2}{\pi d_t^4 \rho Q} \approx \frac{256\mu A_{exit}^2}{\pi d_t^3 \rho Q} \tag{24}$$

If $N << 1$ then most of the pressure drop is over the exit (and the geometry resembles a tank). If $N >> 1$ most of the pressure drop is over the tube length (and the geometry is that of a tube). Taking the hydraulic diameter (d_t) as the characteristic length (l) and substituting reasonable estimates for the physical parameters (A_{exit} is taken from tomography as ¼ of the mean pore-pore area per pore) and the flow rates, values of N for the gas and the liquid are calculated as ranging from 3.0 to 30 for gas and 0.15 to 1.5 for

liquid. The difference between gas and liquid is due to the differences in viscosity and density (equation 24). These estimates are based on average values in order to reduce the level of complexity. Although both the tube and the exit contributions are significant in both cases, this is some indication that the "tank" analogy is more appropriate than the "tube" analogy for the liquid phase, while the "tube" analogy is more appropriate for the gas phase. In the capillary gate model, liquid flow will therefore be modelled as though it takes place in a tank and gas flow as though it takes place in a tube.

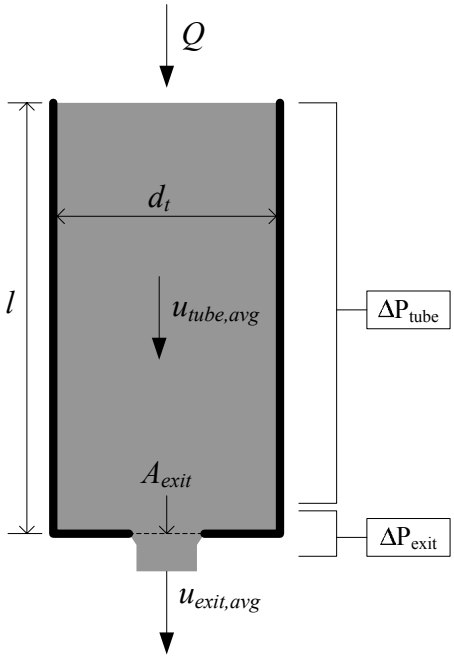

Figure 63. A pore can be approximated as a tube with a constricted exit

Effect of Capillarity on Liquid Flow

The focus is now shifted to how the phenomenological insights in preceding sections are mapped to the packed bed. To start, the effect that capillary action at pore exits have on the liquid flow is dealt with. Consider liquid flow only for a single tank with multiple entrances at the top and bottom (only one of each is shown) as illustrated in Figure 64a. The tank denoted as Tank i receives flow either from other tanks (numbered 1, 2.. K) or from an outside source ($Q_{L,i}$). Flow exits Tank i to tanks numbered 1, 2.. J.

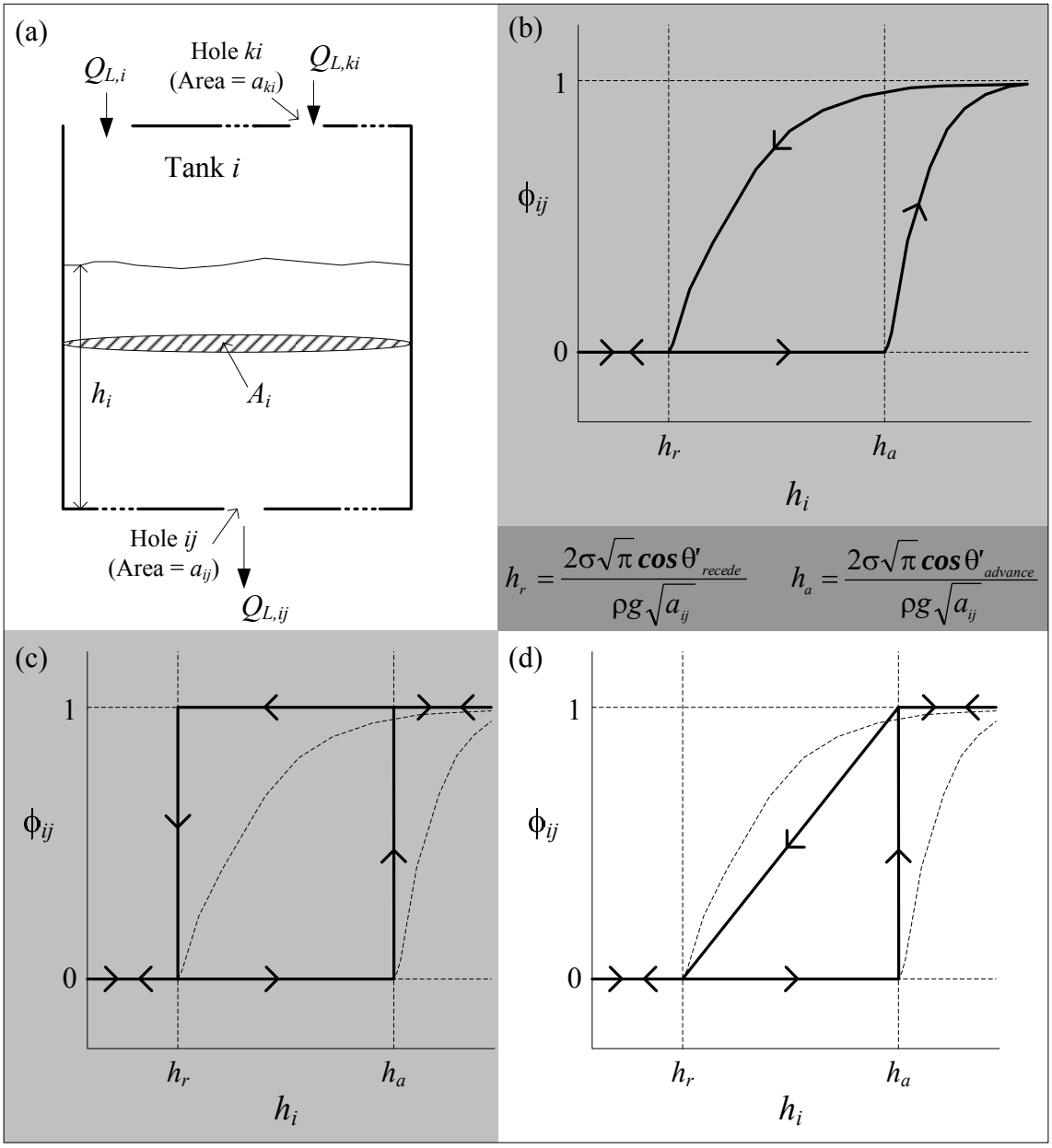

Figure 64. Applying the hydrodynamic multiplicity mechanism to a pore. (a) Single tank geometry, (b) Qualitative plot of the capillary correction factor as a function of liquid height, (c-d) Two approximations of the capillary correction factor as a function of liquid height.

A mass balance on the liquid in Tank *i* reads as (where the constant density of the liquid has been cancelled on both sides of the equation):

$$\frac{dh_i}{dt} = \sum_{k=1}^{K} \frac{Q_{L,ki}}{A_i} - \sum_{j=1}^{J} \frac{Q_{L,ij}}{A_i} + \frac{Q_{L,i}}{A_i} \tag{25a}$$

The relationship between the volumetric flow rate through an exit and the height in the tank is given by equation 23 (with the viscous terms neglected). However, it is now necessary to incorporate capillary action through a factor ϕ_{ij} as follows:

$$\begin{aligned} Q_{L,ij} &= a_{ij}\sqrt{2g}\sqrt{h_i} \quad \text{with no capillary effect} \\ Q_{L,ij} &= a_{ij}\sqrt{2g}\sqrt{h_i\phi_{ij}} \quad \text{with capillary effect included} \end{aligned} \tag{23b}$$

ϕ_{ij} is a factor that accounts for the capillary back-pressure that is present at the tank exit connecting Tank i with Tank j. For a capillary head $h_{c,ij}$ associated with hole ij, ϕ_{ij} is *defined* as:

$$\phi_{ij} = \frac{h_i - h_{c,ij}}{h_i} \quad \text{and} \quad h_{c,ij} = \frac{2\sigma\sqrt{\pi}\,\boldsymbol{cos}\,\theta'}{\rho g\sqrt{a_{ij}}} \tag{26}$$

Note that ϕ_{ij} is always between 0 and 1. In words, the real flow rate through a hole will be smaller than expected because of the presence of the capillary back-pressure. If the capillary back-pressure is greater than the pressure due to the liquid head, there will be no flow and ϕ_{ij} will be equal to zero. When ϕ_{ij} is equal to 1, there are no capillary effects. There are some complexities involved. For example, the angle θ' (in equation 26) evolves dynamically as a function of h_i. Most importantly, ϕ_{ij} fully incorporates the multiplicity effects described in the previous section. To see how, examine Figure 64b, where the relationship between ϕ_{ij} and h_i is shown qualitatively based on visual observations of actual flow through a 1 mm capillary exit. When the head is smaller than h_a (the capillary head associated with the advancing contact angle), there is no flow and ϕ_{ij} is 0. As the head is increased beyond h_a, the contact angle increases asymptotically up to 180 degrees an then stays there. ϕ_{ij} therefore increases gradually and approaches 1 asymptotically. When the flow rate is decreased (remember that flow and head is directly related), the

contact angle decreases gradually back to θ_{rec}, with ϕ_{ij} decreasing to 0 at h_r. It is not known what the exact shapes of these curves are, but two approximations are suggested in Figure 64c and Figure 64d. The first corresponds to neglecting capillary effects once flow is established, while the second assumes that ϕ_{ij} is linear with h_i for the decreasing flow rate leg in the appropriate range. Both approximations yield the same qualitative behaviour and the second approach is adopted because it is believed to be more accurate. ϕ_{ij} is therefore *correlated* as:

$$\phi_{ij} = \begin{cases} 0 \text{ if } h_i < h_r \\ \dfrac{h_i - h_r}{h_a - h_r} \text{ if } h_r < h_i < h_a \text{ and } \dfrac{dh_i}{dt} < 0 \\ 0 \text{ if } h_r < h_i < h_a \text{ and } \dfrac{dh_i}{dt} > 0 \\ 1 \text{ if } h_i > h_a \end{cases} \tag{27}$$

When equation 23b is substituted into the mass balance (equation 25a), it reads:

$$\frac{dh_i}{dt} = \sum_{k=1}^{K} \frac{a_{ki}\sqrt{2g}\sqrt{h_k \phi_{ki}}}{A_i} - \sum_{j=1}^{J} \frac{a_{ij}\sqrt{2g}\sqrt{h_i \phi_{ij}}}{A_i} + \frac{Q_{L,i}}{A_i} \tag{25b}$$

Note that this equation can just as easily be written with Hagen-Poisuielle-type drag terms instead of the Bernoulli terms shown here. Unfortunately, the dynamic behaviour of a single tank does not capture the hydrodynamic behaviour of a packed bed (because there is only one way for the liquid to distribute in the tank). However, consider a system of *three open* tanks as illustrated in Figure 65. Tank 1 has two exits with cross-sectional areas a_{12} leading to tank 2 and a_{13} leading to tank 3 and cylindrical geometry is assumed for both the tanks and the exits. Tanks 2 and 3 have one exit each, with areas of a_{2o} and a_{3o} respectively. The average pore exit area as determined from tomography is approximately 1.3×10^{-6} m^2 with a relative standard deviation of 0.88. We therefore set a_{13} and a_{3o} equal to the average pore exit area and choose a_{12} and a_{2o} to be one standard deviation smaller (i.e. 1.5×10^{-7} m^2). These values are therefore representative of the

packed bed (which is important because they greatly influence the hydrodynamic multiplicity behaviour). The values of the other parameters are given in Table 16 and they have been chosen to represent the system investigated in Chapter 6.

Equation 25b is now written for each tank (with ϕ_{ij} substituted from equation 27), resulting in three ordinary first order non-linear differential equations. Given appropriate initial conditions, the height of liquid in each tank is readily solved for by employing a numerical integration technique.

Table 16. Values of variables used in flow simulation

Variable	**Value(s) used**	**Variable**	**Value(s) used**
A_1, A_2, A_3	5×10^{-6} m^2	ρ	1000 kg/m^3
μ_G	1×10^{-5} m/s^2	P_o	0
θ'_{rec}	95^o (θ_{rec} = 5^o)	σ	0.07 N/m
h_T	0.14 m	$Q_{G,1}$	1×10^{-5} m^3/s (low flow) 13.5×10^{-5} m^3/s (high flow)
a_{small} a_{large}	1.5×10^{-7} m^2 1.3×10^{-6} m^2	$Q_{L,1}$	1×10^{-6} m^3/s (low flow) 2×10^{-6} m^3/s (high flow)
θ'_{crit}	160^o (θ_{adv} = 70^o)		

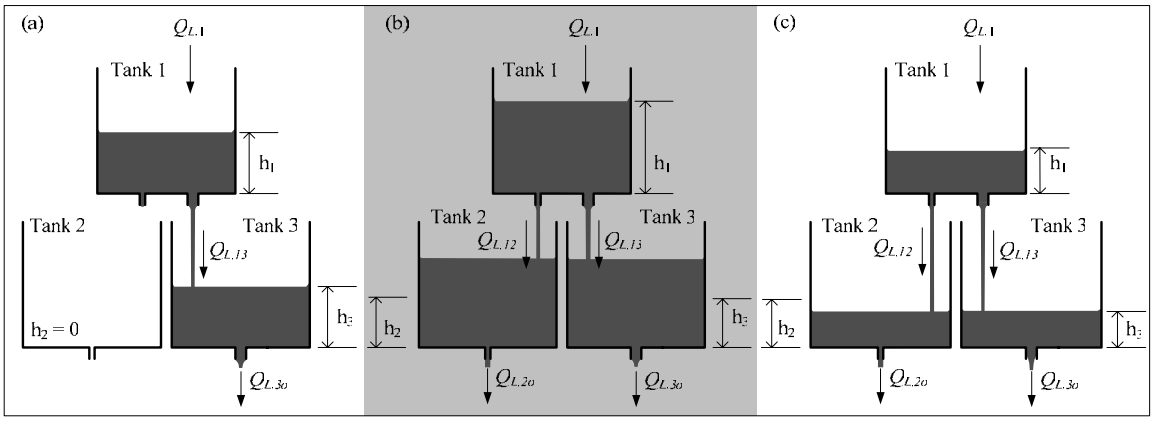

Figure 65. A system of three capillary tanks shows hysteresis akin to that of the packed bed. (a) Low flow condition – increasing leg (b) High flow rate condition (c) Low flow rate condition – decreasing leg.

Note that because the ϕ_{ij} parameter changes abruptly at different values of h_i, some numerical problems may be encountered when the usual solvers (e.g. Runge-Kutta) are used since these solvers do not expect such abrupt changes. Instead, it is recommended that an adaptive mesh be used for the temporal discretization, where smaller time steps are employed in the vicinity of detected ϕ_{ij} changes.

As an example of how a hydrodynamic multiplicity trend can be captured by this relatively simple model, a liquid flow rate variation induced hysteresis loop is executed – results shown in Figure 66. The initial h_i in each tank is specified as zero. The flow rate to Tank 1 is then increased to the low flow condition ($Q_{L,1}$=1×10^{-6} m^3/s) and steady state is established (point A). The flow is increased to the high flow condition ($Q_{L,1}$=3×10^{-6} m^3/s) and then decreased back to the low flow condition, and steady state is again established (point C). The numerical values of these flow rates were chosen for illustrative purposes because the actual flow rate through a pore is difficult to estimate.

Starting from time zero, when flow is introduced the level in Tank 1 rises. There is at this stage no flow through holes 12 or 13 to Tanks 2 or 3. When the height in Tank 1 (h_1) exceeds $h_{a,13}$ (the blue dashed line), hole 13 opens and liquid flows into Tank 3.

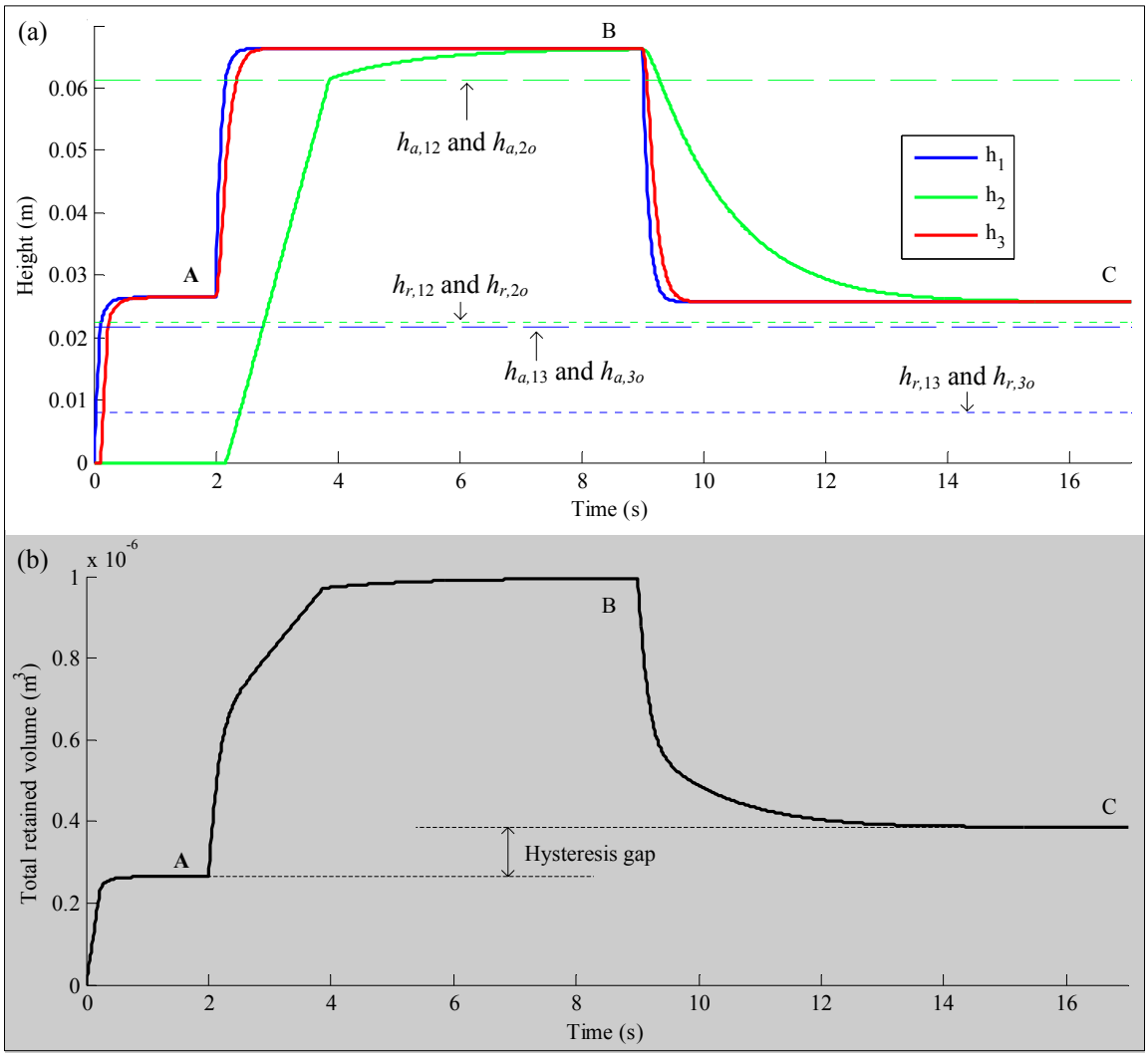

Figure 66. A liquid flow rate variation induced hysteresis loop for the model system. (a) Height in each tank. (b) Total retained volume. Point A corresponds to the illustration in Figure 65a, point B with Figure 65b and point C with Figure 65c. Note that the total retained volume (the analogue of holdup) is higher at point C than at point A.

As soon as h_3 exceeds the same value liquid starts draining from Tank 3 and steady state (point A) is reached within about 2 seconds. Note that h_1 does not exceed $h_{a,12}$ (the dashed green line) and so hole 12 does not open. Tank 2 remains dry. When the feed flow rate is increased, hole 12 does open (when $h_1 > h_{a,12}$) and shortly after (when $h_2 > h_{a,2o}$) so does hole 2*o*. When the flow rate is reduced again, all four holes remain open (because $h_1 > h_{r,12}$, $h_1 > h_{r,13}$, $h_2 > h_{r,2o}$ and $h_3 > h_{r,3o}$) and a different steady state is achieved (point C). Despite the fact that both h_1 and h_3 is smaller at C than they were at A (not apparent in

the figure), the additional volume retained in Tank 2 at point C causes the total retained volume to be higher at C than at A (Figure 66b). This is exactly what is seen in a liquid flow rate variation induced holdup hysteresis loop in trickle flow (when comparing the Kan-Liquid and Non-pre-wetted modes). Note that the fact that the three tank levels are equal at steady state is because holes 12 and 2*o* and holes 13 and 3*o* were assumed to be equal in size (this will not generally be the case). Before extracting the other hydrodynamic trends, it is prudent to incorporate the effects of gas flow first.

Effect of Capillarity on Gas Flow

The effect of capillarity in gas flow is handled similarly to that of liquid flow through the introduction of a correction factor (ψ_{ij}). However, some changes to the geometry of the three tanks first need to be made in order to properly evaluate the pressure drop (as shown in Figure 67). The tanks are closed off at a height of h_T and gas is fed at a flow rate of $Q_{G,1}$ to Tank 1. Some additional connections are made: Tank 1 is connected to Tank 2 and Tank 3 with holes of large diameter ($a_{G,12} = a_{G,13} = a_{L,13} = a_{L,3o} = 1.3 \times 10^{-6}$ m^2) and to the outside with a hole of small diameter ($a_{G,1o} = a_{L,12} = a_{L,2o} = 1.5 \times 10^{-7}$ m^2). Tanks 2 and 3 are connected with the outside with one large hole each ($a_{G,2o} = a_{G,3o} = 1.3 \times 10^{-6}$ m^2). Note that only two hole diameters are used, a large one equal to the average hole diameter as measured in Chapter 6 and one small one equal to the average diameter minus one standard deviation.

Recall that gas flow is to be treated as flow in a tube as governed by the viscous (Hagen-Poisuielle) drag term in equation 26. Neglecting the gas head, the flow rate of gas between two tanks are related to the difference in pressure as follows:

$$\Delta P = P_i - P_j = \frac{128\mu_G Q_{G,ij} l}{\pi d_t^4}, \text{ or}$$

$$Q_{G,ij} = \frac{(P_i - P)\pi d_t^4}{128\mu_G l} \approx \frac{(P_i - P)\pi d_t^3}{128\mu_G} \approx \frac{C(P_i - P)\pi(h_T - h_i)^3}{128\mu_G} \quad \text{no capillarity} \tag{28a}$$

$$Q_{G,ij} = \frac{C(P_i - P)\pi(h_T - h_i)^3 \psi_{ij}}{128\mu_G} \quad \text{with capillarity} \tag{28b}$$

Here, the characteristic length and tube diameters are both assumed to be the hydraulic diameter of the space above the liquid in the tank (C is a constant that depends on the value of A_i only – it is roughly equal to 5×10^{-8} for present conditions). Note that the gas capillary correction factor (ψ_{ij}) has been incorporated in equation 28b. It is there because for pre-wetted beds the gas exits will be clogged with liquid and a capillary threshold ($P_{crit,ij}$) will need to be crossed before gas flow can commence through the hole. Once the hole is open however, there is no capillary back-pressure and the hole never closes again. This means that unlike ϕ_{ij}, ψ_{ij} will be *either* 1 or 0. This corresponds to the "liquid-bridged" condition of Melli & Scriven (1991).

A small change to the liquid momentum relation (equation 23b) is also necessary once a pressure drop exists between the tanks. Note that the gas pressure in each tank adds an additional head to the liquid and should be included in the flow relations, i.e.:

$$Q_{L,ij} = a_{ij}\sqrt{\phi_{ij}\left[2gh_i + \frac{2(P_i - P_j)}{\rho_L}\right]} \tag{29}$$

For each tank, a mass balance is derived assuming incompressible flow and the momentum relations (equations 28b and 29) are substituted. The generic equations of the final model are:

Liquid :

$$\frac{dh_i}{dt} = \sum_{k=1}^{K} \frac{a_{L,ki}}{A_i} \sqrt{\phi_{ki}\left[2gh_k + \frac{2\left(P_k - P_i\right)}{\rho_L}\right]} - \sum_{j=1}^{J} \frac{a_{L,ij}}{A_i} \sqrt{\phi_{ij}\left[2gh_i + \frac{2\left(P_i - P_j\right)}{\rho_L}\right]} + \frac{Q_{L,i}}{A_i} \tag{30}$$

Gas :

$$-\frac{dh_i}{dt} = \sum_{k=1}^{K} \frac{C\pi\left(P_k - P_i\right)\left(h_T - h_k\right)^3 \psi_{ki}}{128\mu_G A_i} - \sum_{j=1}^{J} \frac{C\pi\left(P_i - P_j\right)\left(h_T - h_i\right)^3 \psi_{ij}}{128\mu_G A_i} + \frac{Q_{G,i}}{A_i} \tag{31}$$

Capillary Correction :

$$P_{crit,ij} = \frac{-2\sigma\sqrt{\pi}\cos\theta'_{crit}}{\sqrt{a_{L,ij}}}$$

$$P_{rec,ij} = \frac{-2\sigma\sqrt{\pi}\cos\theta'_{rec}}{\sqrt{a_{L,ij}}}$$

$$\phi_{ij}\left(t_{now}\right) = \begin{cases} 0 \text{ if } \left[\rho_L g h_i + \left(P_i - P_j\right)\right] < P_{rec,ij} \\ \dfrac{\left[\rho_L g h_i + \left(P_i - P_j\right)\right] - P_{rec,ij}}{P_{crit,ij} - P_{rec,ij}} \text{ if } P_{rec,ij} < \left[\rho_L g h_i + \left(P_i - P_j\right)\right] < P_{crit,ij} \text{ and } \dfrac{dh_i}{dt} < 0 \\ 0 \text{ if } P_{rec,ij} < \left[\rho_L g h_i + \left(P_i - P_j\right)\right] < P_{crit,ij} \text{ and } \dfrac{dh_i}{dt} > 0 \\ 1 \text{ if } \left[\rho_L g h_i + \left(P_i - P_j\right)\right] > P_{crit,ij} \end{cases} \tag{32}$$

$$\psi_{ij}\left(t_{now}\right) = \begin{cases} 0 \text{ if } \left(P_i - P_j\right) < \dfrac{-2\sigma\sqrt{\pi}\cos\theta'_{crit}}{\sqrt{a_{G,ij}}} \text{ and } \psi_{ij}\left(t < t_{now}\right) \neq 1 \\ 1 \text{ if } \left(P_i - P_j\right) \geq \dfrac{-2\sigma\sqrt{\pi}\cos\theta'_{crit}}{\sqrt{a_{G,ij}}} \text{ or } \psi_{ij}\left(t < t_{now}\right) = 1 \end{cases}$$

Model parameters are reported in Table 16. From these 6 equations it is possible to solve for the three tank heights (h_1, h_2 and h_3) and the three pressures (P_1, P_2 and P_3). The system's liquid saturation and system pressure drop can be calculated from these values. It is possible to specify various flow histories (to yield hysteresis loops) or initial conditions (to yield different pre-wetting modes). This model also captures the well known hydrodynamic trends that are not multiplicity related – namely that pressure drop

increases with both liquid and gas velocity, while holdup increases with liquid velocity but decreases with gas velocity.

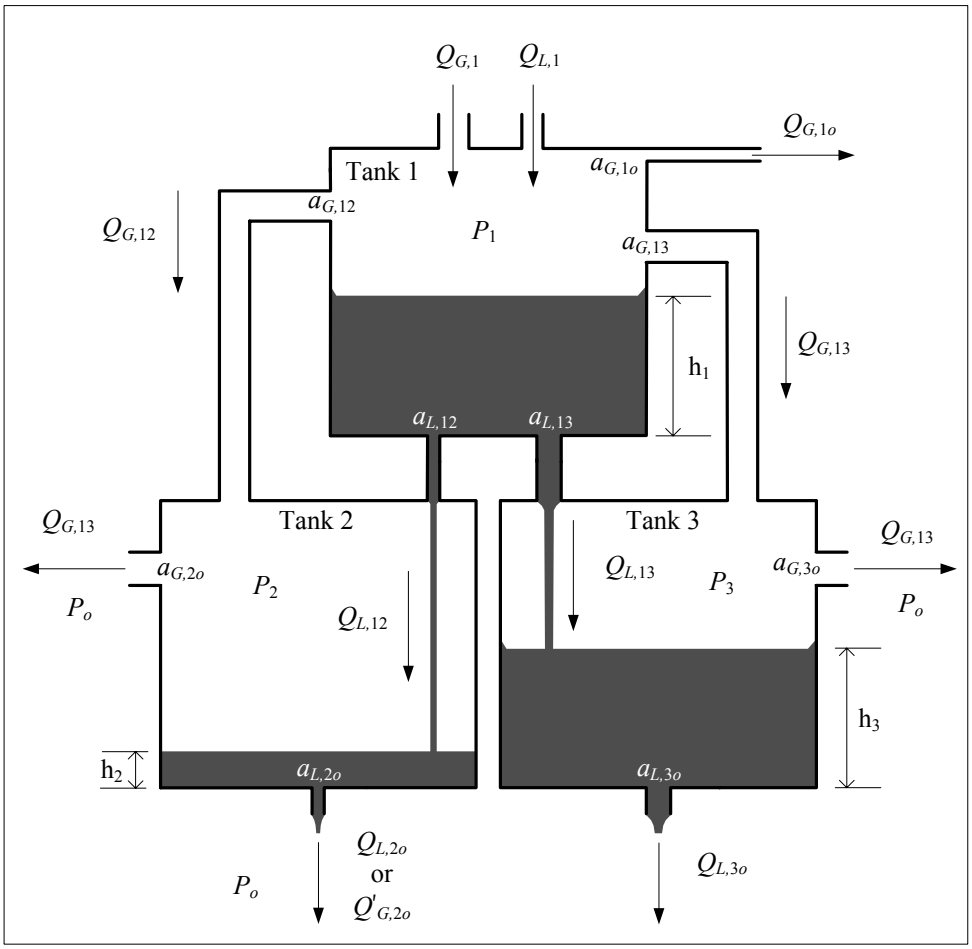

Figure 67. The proposed hydrodynamic model for gas and liquid flow.

7.3.2 Model Performance and Characteristics

The efficacy of the proposed model to qualitatively represent the hydrodynamic multiplicity trends is illustrated by instigating the following experimental plan on the model. Notice that this plan closely represents the actual experimental plan that was adopted to generate the data in earlier chapters according to the conceptual framework identified in Chapter 2. Model performance is illustrated in Figure 68 along with the calculated saturation and pressure drop values.

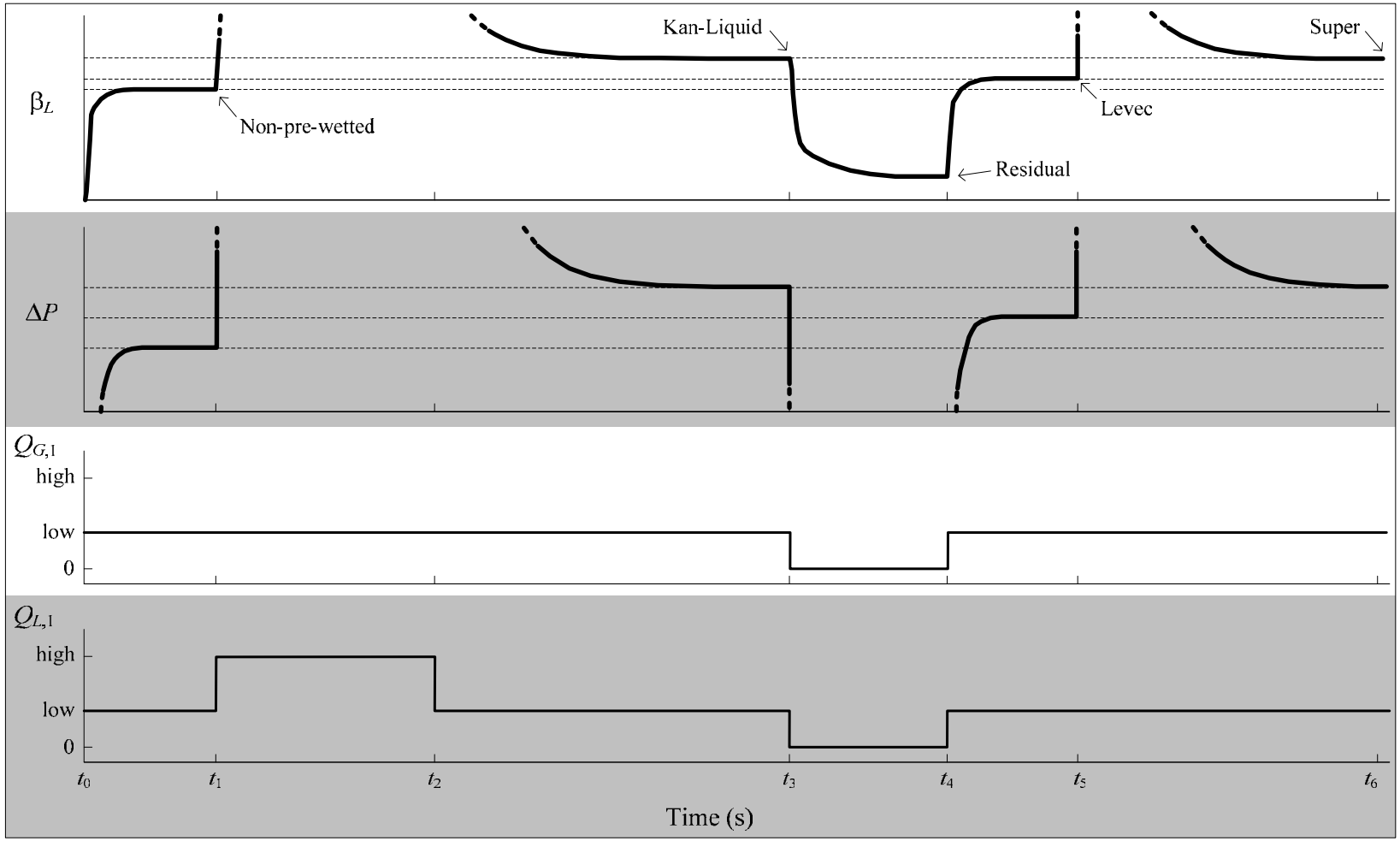

Figure 68. Model performance: dynamic evolution of saturation and pressure drop with liquid flow rate changes

(i) The initial values for all three tank heights are set to zero (i.e. zero saturation). The initial pressures in all three tanks are set to zero (t_0).

(ii) Gas and liquid flow is introduced at the *low* velocities and the simulation continues until steady state has been achieved. This corresponds to the Non-pre-wetted mode (t_1).

(iii) The liquid flow rate is increased to *high* while keeping the gas flow rate at *low* and steady state is achieved (t_2).

(iv) The liquid flow rate is reduced to *low* (gas flow rate still at *low*) and steady state is achieved. This corresponds to the Kan-Liquid mode (t_3).

(v) The liquid and gas flow rates are reduced to zero and the system drains under gravity – this yields the residual holdup (t_4).

(vi) The flow rates are increased back to the *low* value and steady state is achieved. This corresponds to the Levec mode (t_5).

(vii) The simulation is now restarted with flow rates set at *low*, but with the important difference of specifying the initial tank heights equal to 90% of their maximum values (i.e. $\beta_L = 0.9$). Draining now continues under irrigation until steady state is established, i.e. the Super mode (t_6).

The model performance closely resembles the actual experiment both in holdup and in pressure drop (refer back to Figure 34a). When liquid flow is initiated at t_0, the capillary threshold for flow through liquid hole 13 ($P_{crit,13}$) is quickly reached and steady state is established without liquid hole 12 being opened. When the liquid flow rate is increased to the *high* value at t_1, $P_{crit,12}$ is exceeded and liquid flows through both hole 12 and 13. When the flow rate is reduced back to low, the total pressure head is below $P_{crit,12}$ but above $P_{rec,ij}$, and both holes remain open. The new steady state is the Kan-Liquid mode and the total retained volume (saturation) is higher. Next, gas and liquid flow is shut off (at t_3) and the tanks drain. However, the holes close for flow when $P_{rec,ij}$ is reached and a height of liquid is retained at zero flow. This is the residual holdup. When flow is re-started at t_4, holes 13 and 3*o* soon open for flow but the pressure head in Tank 1 remains

below $P_{crit,12}$ and Tank 2 therefore does not receive any flow. The combined saturation of all three tanks is higher than the Non-pre-wetted mode but lower than the Kan-Liquid mode. This is the Levec mode. Lastly, when the saturation in each tank is set at a high value and drained under irrigation, both hole 12 and 13 are open and remain open because the steady state heights exceed $P_{rec,12}$. This is the Super mode. Note that flooding and draining under irrigation has exactly the same effect as increasing and decreasing the tank heights by increasing and decreasing the flow rate. This explains why the Kan-Liquid and Super modes yielded such similar results in Chapters 4, 5 and 6. Note also that most previous hydrodynamic models failed to converge to the residual holdup in the limit of zero liquid velocity. This is because these models do not take adequate account of the capillary effect. Figure 68 also illustrates the dynamics of establishing the different modes. The Levec mode reaches steady-state very quickly while the Kan-Liquid modes takes much longer (in the simulation above the Kan-Liquid mode took approximately 5 times as long as the Levec mode to reach steady state). Compare this with the results of Figure 34b. De-saturation (Kan-Liquid) takes longer than saturation (Levec) because the liquid leaves the tanks at slower rates than it enters the tank (before steady state is established).

A further illustration of the efficacy of the model is shown in Figure 69, where the liquid distribution in the three tanks is shown along with the discharge rates of Tanks 2 and 3. Note that the liquid distribution is bi-modal in the Levec mode (Tanks 1 and 3 have high holdup and Tank 2 has a low holdup) and uni-modal in the Kan-Liquid mode (all three tanks have the same holdup). Note that the idea of rivulet and film flow is also represented. A rivulet is a series of connected tanks (pores) with high holdup together with tanks (pores) with very low holdup (as seen in the Levec mode). Film flow corresponds to the fact that all tanks (pores) in the Kan-Liquid mode have a (lower) uniform holdup. These observations agree with those in the previous chapter and also with the similar investigations of Lutran et al. (1991) and Sederman & Gladden (2001). Cross-sectional holdup maldistribution is another manifestation of this effect.

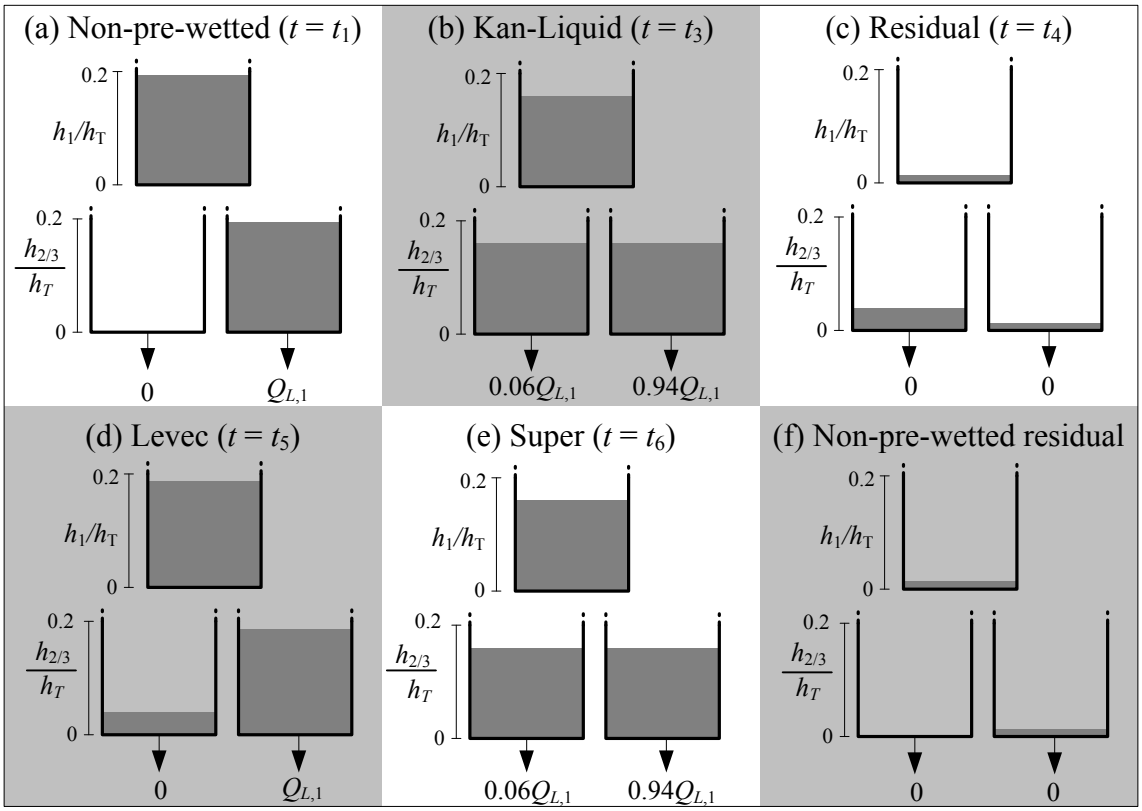

Figure 69. Liquid distribution by tank for the simulation shown in Figure 68.

The model also captures the liquid exit flux distribution differences between the modes, namely that the liquid exits more uniformly in the case of the Kan-liquid mode than in the Levec or Non-pre-wetted modes. This agrees qualitatively with the data of Ravindra et al. (1997b).

Note that this evaluation is not restricted to the limiting cases. In general, any incremental increase in liquid velocity will increase holdup and more and more holes will open for flow. This is the mechanism by which new rivulets are created.

As an interesting aside, the residual liquid distribution is shown in Figure 69c. Note that there is a lot of liquid in Tank 2 and very little in Tanks 1 and 3. The heights correspond to the capillary head for the exit. In an early study (Van der Merwe et. al., 2004), we showed by photography that the residual holdup is held in mainly two forms: small volume pendular rings (Tanks 1 and 3), and large volume "globules" at locations where

the local porosity is low (i.e. small pores, Tank 2). It is satisfying that the present model also captures these observations qualitatively. Secondly, note that when the liquid and gas flow is interrupted after operation in the Non-pre-wetted mode, the residual holdup will be much smaller and distributed as shown in Figure 69f. The fraction of residual holdup after the Non-pre-wetted mode to the residual holdup after flooding gives one a qualitative indication of the number of active pores. Similarly, the residual holdup in Tank 2 is not contacted by liquid in the Levec mode. In the Kan-Liquid and Super modes all the residual holdup is contacted. In a preliminary study (Van der Merwe & Nicol, 2005), we measured these "active residual" holdup fractions at different flow rates and found the same qualitative trends as exhibited by the present model. The fact that gates close at very low velocity was also seen in the fact that the volumetric utilization coefficient was below 1 in the Super mode only at very low velocities (< 2 mm/s) and increased with increasing liquid velocity.

It is equally important for the same capillary mechanism to represent the effect of changes in gas flow rate on the system. A major question that has not been addressed is the fact that a gas velocity variation induced hysteresis loop causes a Kan-Liquid mode to have a higher holdup but lower pressure drop, while it causes the Levec mode to have both higher holdup and higher pressure drop. The results of applying such gas flow rate changes to the model are shown in Figure 70. Consider that for pre-wetted beds before gas flow is introduced, the holes marked $a_{G,13}$, $a_{G,12}$, and $a_{G,1o}$ are all likely to be filled with liquid and are therefore closed by capillary action. When gas flow is turned on, the pressure in Tank 1 will rise until it exceeds the capillary threshold $P_{crit,13}$ at which point hole 13 will open and the liquid will be discharged. The hole then remains open since the liquid does not re-establish itself. Now, the same reasoning applies to the other large gas-carrying holes and these all open as well ($\psi_{12} = \psi_{12} = \psi_{2o} = \psi_{3o} = 1$). However smaller holes will only open when the pressure exceeds their capillary counter-pressures (that are higher than those of the large holes).

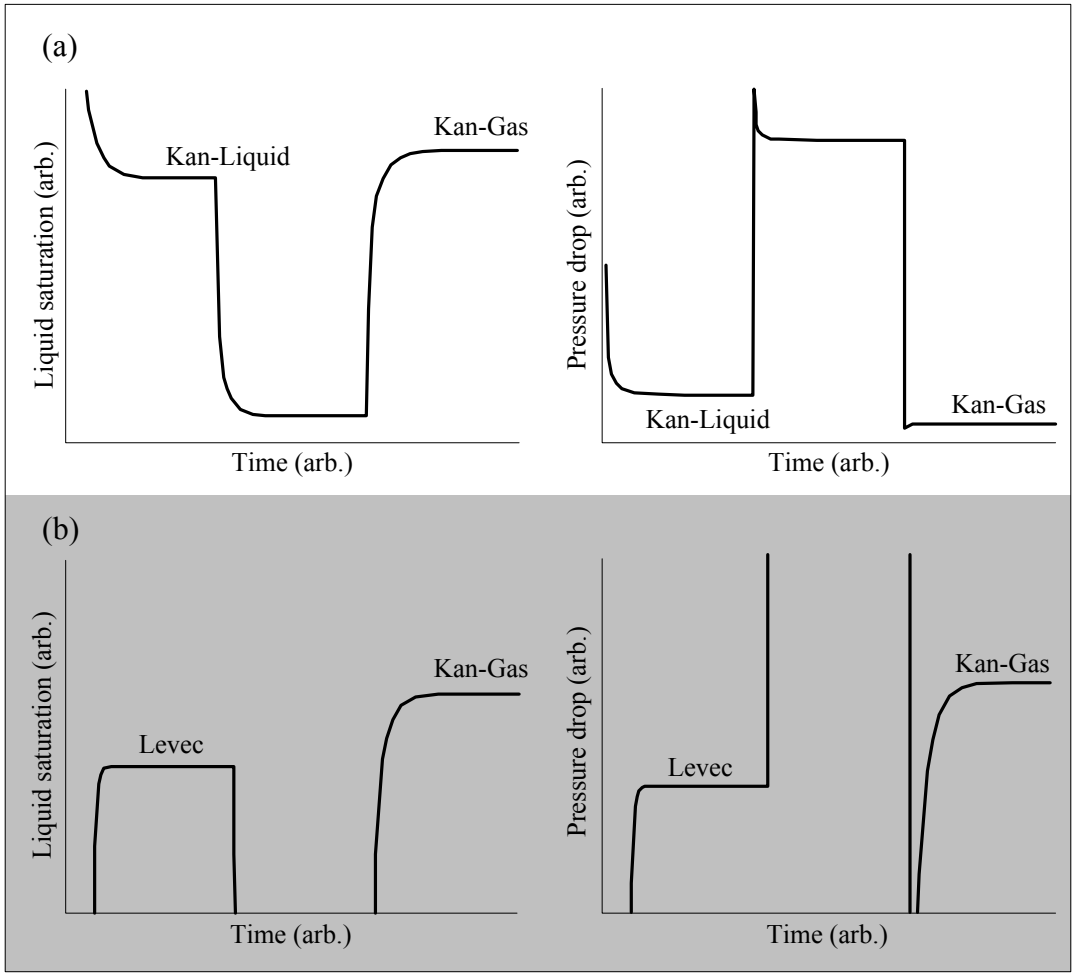

Figure 70. Gas flow rate variation induced hysteresis starting from the (a) Kan-Liquid mode and (b) Levec mode.

It was found that only one smaller hole (gas hole 1*o*) needed to be included in the model to account for gas flow rate variation induced hysteresis. Starting from the Kan-Liquid mode, the large gas holes are open for flow, but the small one is not. When gas flow is increased, a stage is reached where the pressure in Tank 1 exceeds the critical value for hole 1*o* to open for gas flow. When the gas flow is reduced, the hole remains open. At the original gas velocity, the gas now has an additional escape route and the pressure in Tank 1 is lower (total pressure drop is lower). Consequently, the pressure head on the liquid is also smaller resulting in higher saturations (higher holdup). The limiting case of this effect is the Kan-Gas mode. This corresponds closely to the original postulate of Kan &

Greenfield (1979) who suggested that the high gas velocity results in the creation of additional gas pathways (and a consequent decrease in the average gas tortuosity). Off course, the increased gas velocity has a second effect, namely that it results in higher pressure drops that add to the pressure head above the liquid exits. In the Levec mode hole $a_{L,12}$ was closed. A high gas velocity can cause the total pressure head (liquid head plus pressure difference between Tanks 1 and 2) to exceed the capillary threshold ($P_{crit,12}$) even though the liquid head has decreased. Hole 12 will open for liquid flow and remain open even as the gas velocity is decreased back to the original value (provided that the total pressure head exceeds $P_{rec,12}$). The result is that both liquid saturation and pressure drop is higher than before. The existence of different sized gas holes along with the capillary mechanism therefore sufficiently accounts for gas flow rate variation induced hysteresis.

The illustrations above have primarily addressed trends **(A), (B), (C), (F)**, **(G)**, **(I), (Q)** and **(S)**. However, the capillary gate model also provides rationalizations for the other trends as follows (they are not illustrated or discussed in as much detail for the sake of brevity):

- **(D)** Larger particles do not exhibit as much hysteresis because their pore exits are larger in size (despite the fact that porosity is the same) and therefore have lower capillary thresholds that are more easily crossed.
- **(E)** Wetting efficiency is lower in the Levec mode because the liquid is maldistributed.
- **(H)** The gas-liquid area follows the liquid holdup trends.
- **(J)** Small flow rate changes have little effect after the first cycle because the first cycle opens those holes that are near $P_{crit,ij}$. They do not close in the low flow condition because the total pressure head was near $P_{crit,ij}$ (i.e. higher than $P_{rec,ij}$).
- **(K)** Decreasing the surface tension lowers the pulsing boundary because the critical capillary threshold decreases – making it easier to cross.

(L) A temporary decrease in surface tension does not affect the Kan-Liquid mode because all the holes are already open for flow. It does however open up holes in the Levec mode that do not close again (because the total pressure head exceeds $P_{rec,ij}$ but not $P_{crit,ij}$).

(M) Porous particles show less hysteresis because the difference between receding and advancing contact angles are smaller.

(N) The pulsing boundary is associated with the extent of hysteresis because reaching the pulsing boundary at lower velocity means that it is easier to cross all the capillary thresholds (and hysteresis is therefore diminished).

(O) The pressure drop increases drastically with increasing gas or liquid velocity in the Levec mode (at high pressure) because more and more pores participate in liquid flow as holes are opened with increasing velocity. At lower pressures, the lower pressure drop means that holes are not as easily opened and the efect is smaller. In the Kan-Liquid mode, all the holes are already open and the effect of more participating pores is absent.

(P) At high pressures the pressure drop is high (it scales with the density of the gas) and it is easier to cross the capillary thresholds. This is especially true at high u_L, where the high holdup causes high pressure drop. The result is that the holes open at lower velocity and therefore a lower extent of multiplicity is observed at a given velocity. Note that both the experiments in Chapter 4 and the model indicates that pressure drop determines the extent of hydrodynamic multiplicity.

(R) The small saturation changes in the Levec mode are pores that are close to one of the capillary thresholds (P_{crit} for saturation and P_{rec} for de-saturation). Any small disturbance may cause the threshold to be crossed. Note that the scale of these changes were approximately 1 particle diameter – i.e. approximately the size of a pore (see pore size distribution), and similar in shape to the pores identified in Chapter 6. The difference maps of Chapter 5 are therefore a direct visualization of the capillary mechanism in action (pore heights crossing the capillary thresholds).

(T) The fraction dry (bar residual holdup) pores in the Levec mode decreases with both u_L and u_G because both these increase the total pressure head (u_G increases the pressure drop more than it decreases the holdup), which opens more holes.

7.3.3 Detractions, Limitations, Validations and Extensions

This model is intended as an example of how the capillary mechanism leads to the observed behaviour and not as a quantitative tool. The major limitation of the model therefore is its qualitative nature. The central idea here is that liquid distribution is governed by the requirement that a capillary threshold need to be crossed before liquid can flow from pore to pore and that this threshold exhibits hysteresis itself. It is not difficult to see that this idea can be incorporated into larger pore networks and most of the existing hydrodynamic models. For example, the slit model can be extended to a network-of-slits model where each pore is then represented as a slit. Liquid and gas access to slits can then be governed by the capillary mechanism. Similarly, Jiang et al. (1999) already proposed that capillary pressure be incorporated into a CFD or DCM type description. However, there is ample indication in this work that the fundamental unit of a trickle bed (by which the mass and momentum conservation equations are to be derived) is the pore (and not a homogeneous cell). In this regard, it is necessary to emphasize that hydrodynamic multiplicity through the proposed mechanism arises only because there are dissimilarities between the pores. More specifically, the pore exits vary in size. The tomographical analysis of Chapter 6 allows us to determine that this is indeed the case (Figure 71a).

Note also that the model assumes that all exits are either gas- or liquid-filled – there are no two-phase flow through any of the exits. This simplification is supported by the actual measured pore exit filling fractions shown in Figure 71b. It shows two clear peaks at 0 (gas-filled) and 1 (liquid-filled), although some two-phase flow also occur.

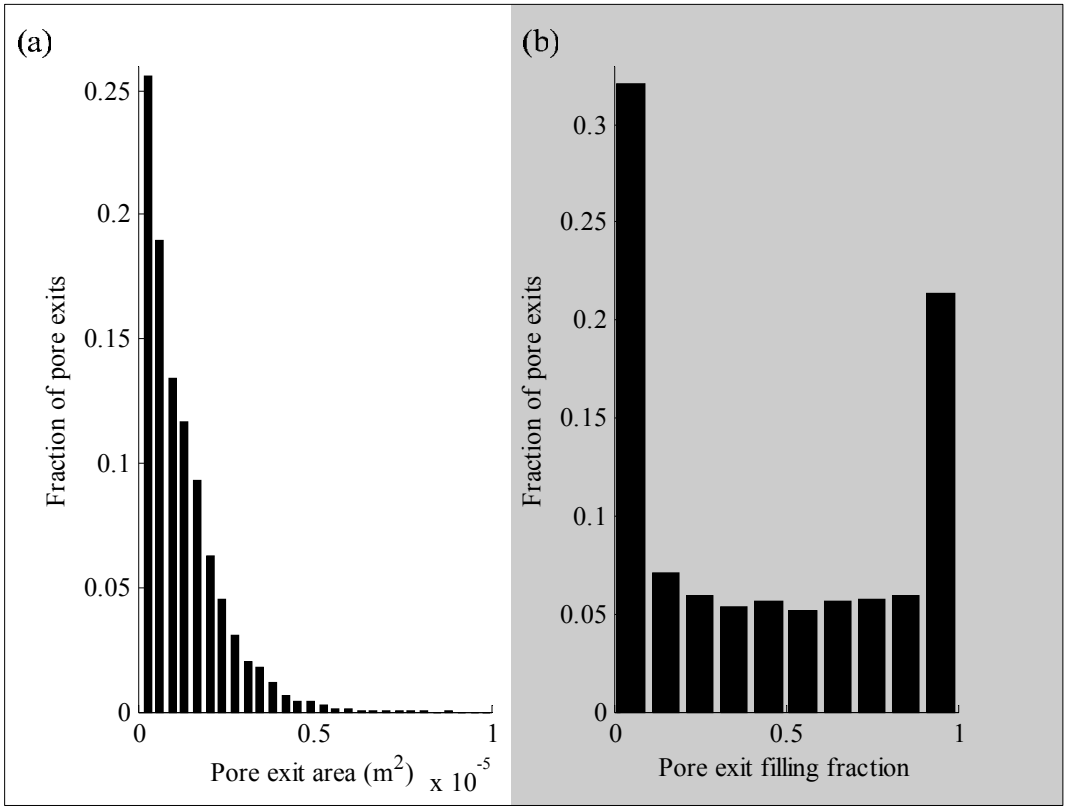

Figure 71. Pore exit statistics. (a) Pore exit area distribution (b) Pore exit filling fraction (Levec mode at u_L = 5.3 mm/s, u_G = 4.7 cm/s – other conditions look similar).

A further limitation of this study is that the dispersion characteristics of the model and the trickle bed have not been compared. Also, the interfacial areas cannot be calculated directly from the model. A possible exception may be wetting efficiency. Note that in adopting the cylindrical tank geometry, it was implicitly assumed that wetting efficiency is directly proportional to holdup (saturation). To see this, note that the wetting efficiency of the three tanks increases linearly with tank height. Again, the tomographical analysis can be used to support this approach (Figure 72).

A final observation regarding the validity of the assumed operating variable values in Table 16 is necessary. The volumetric flow rates and total tank height were chosen to illustrate the trends that can be extracted from the model, and not to represent the individual pores. The height is particularly large and physically unrealistic.

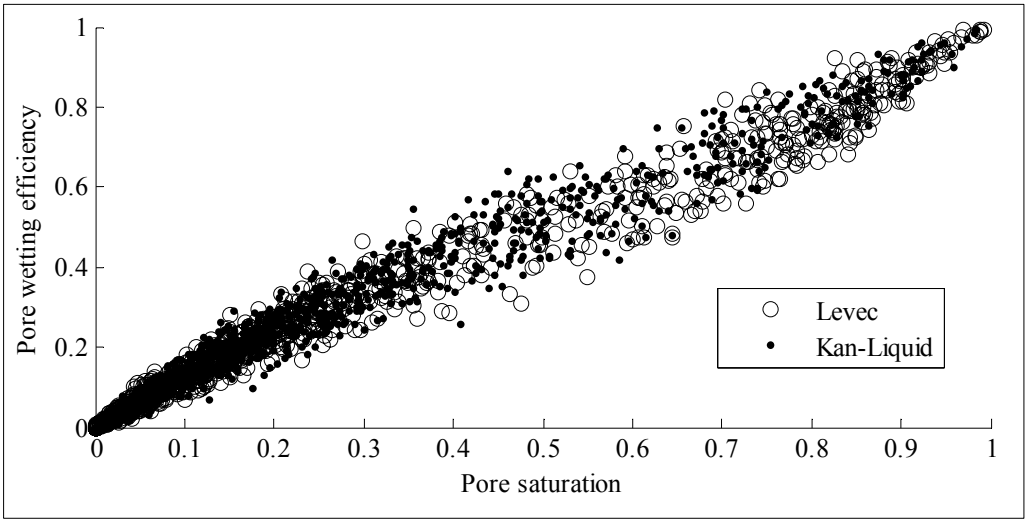

Figure 72. Pore wetting efficiency as a function of pore holdup from tomography. Note the nearly linear relationship (u_L = 2.7 mm/s, u_G = 4.7 cm/s). Other conditions show similar behaviour.

Of course, the total height necessary to illustrate the model performance is a function of the total pore exit area. For the real geometry, the pore coordination numbers are larger (mean of 11), which means that the liquid heights will all be much smaller. However, in the model a coordination number of 2 is chosen in order to keep it simple. Note also that, in reality, the capillary back-pressure at the pore exits is a function of the length of the gas-liquid-solid contact line, which is likely to be longer than the circumference of the hole (because of the geometry of the liquid held in the neck). This too will reduce the tank heights to more realistic values. These effects are severely complicated and are considered beyond the present scope.

In conclusion, the model has been developed based on the existing data in literature and the new experimental insights in Chapters 2, 4, 5 and 6. The model agrees qualitatively with all the observed trends and shows the potential to be incorporated into larger pore network models or alternative approaches like CFD or phenomenological models.

7.4 Conclusion

This chapter introduced a pore-scale capillary mechanism based on the original suggestion that contact angle hysteresis is the controlling phenomenon (Levec et al., 1986). The mechanism dictates which pores receive flow. When properly incorporated into a hydrodynamic model, it accounts for the observed hydrodynamic behaviour. Table 17 summarises the model's ability to qualitatively represent the experimentally observed hydrodynamic multiplicity trends.

Table 17. Comparison between observed multiplicity trends and model capability

Trend number	Description	Model able to represent this trend?
(A)	New rivulets are created as u_L increases, rivulet vs. film flow patterns	Yes
(B)	Liquid flow rate variation induced hysteresis in each mode	Yes
(C)	Gas flow rate variation induced hysteresis (particularly the opposite effect on Levec and Kan-Liquid/Super modes)	Yes
(D)	Lower extent of multiplicity for larger particles	Yes
(E)	Lower wetting in Levec mode, bi-modal distribution	Yes
(F)	Holdup increases in the order Non-pre-wetted, Levec, Kan-Liquid/Super, Kan-Gas	Yes
(G)	Pressure drop increases in the order Non-pre-wetted/Levec, Kan-Gas, Kan-Liquid/Super	Yes
(H)	Gas-liquid mass transfer coefficient hysteresis	Yes
(I)	Similarity between Kan-Liquid and Super modes	Yes
(J)	Small flow rate changes have no effect after the first cycle	Yes
(K)	Lower surface tension lowers the extent of multiplicity	Yes
(L)	Surface tension variation induced hysteresis	Yes
(M)	Porous	Yes
(N)	Boundary	Yes
(O)	Differences in functional pressure drop vs. u_L behaviour in different modes at high P	Yes
(P)	Pressure drop determines extent of multiplicity	Yes
(Q)	Kan-Liquid takes longer to reach steady state than Levec	Yes
(R)	Pore-scale low frequency instability in Levec mode	Yes
(S)	Holdup distribution by pore different in different modes	Yes
(T)	Fraction of dry pores behaviour vs. u_L and u_G by mode	Yes

Note that although the detailed tomographic analysis of Chapter 6 contributes only two trends, the results of that investigation were used extensively in the identification,

development and validation of the proposed mechanism. The key feature is that the analysis provides high definition 3D images that allow *pore-scale* statistics to be calculated. The importance of modelling trickle flow multiplicity at the pore-scale is evident throughout the latter parts of this work.

In so far as hydrodynamic multiplicity modelling is concerned, it is recommended that future studies address the issue of quantitative prediction (possibly by incorporating the capillary mechanism into pore-network or discrete-cell models). Although this seems relatively straightforward, present attempts showed that the additional complexity in the pore-geometry, pore-connection structure and pore-scale flow patterns will introduce parameters that can only be correlated empirically (and will therefore require new insights or a larger experimental database). It is believed that the qualitative insights offered in this chapter will in future contribute to the development of a fully predictive hydrodynamic multiplicity model.

It is further recommended that the important issue of the impact of hydrodynamic multiplicity on trickle bed reactor performance should also be evaluated, experimentally and theoretically, by future investigators. The next chapter presents data and ideas that highlight the way forward in this regard.